Topology optimization of nonlinear structural dynamics with invariant manifold-based reduced order models

Pozzi, Matteo; Marconi, Jacopo; Jain, Shobhit; Li, Mingwu; Braghin, Francesco

DOI
10.1007/s00158-025-04010-1

Publication date
2025

Document Version
Final published version

Published in
Structural and Multidisciplinary Optimization

Structural and Multidisciplinary Optimization (2025) 68:72
https://doi.org/10.1007/s00158-025-04010-1

RESEARCH PAPER

Topology optimization of nonlinear structural dynamics with invariant manifold-based reduced order models

Matteo Pozzi[1] · Jacopo Marconi[1] · Shobhit Jain[2] · Mingwu Li[3] · Francesco Braghin[1]

Received: 4 November 2024 / Revised: 25 March 2025 / Accepted: 26 March 2025

Abstract

We present a structural topology optimization method to tailor the hardening/softening dynamic response of nonlinear mechanical systems. The coefficient that controls this behavior is computed *analytically* using the third-order normal-form parametrization of the Lyapunov subcenter manifold, which eliminates the need for expensive full-order simulations and numerical continuation to approximate the so-called *backbone curve* of the system. The method further leverages the *adjoint method* for efficiently computing sensitivities of the objective function and constraints, while the explicit formulation of nonlinear internal elastic forces through tensor notation simplifies these evaluations. Notably, this *tensorial approach* is computationally efficient, especially when applied to a regular grid of elements. Consequently, the proposed approach offers a robust and efficient framework for optimizing the dynamic performance of nonlinear mechanical structures modeled with high-dimensional finite element models. The findings are corroborated through examples of two geometrically nonlinear systems, a Messerschmitt-Bölkow-Blohm (MBB) beam and a microelectro-mechanical system (MEMS) inertial resonator.

Keywords Topology optimization · Nonlinear structural dynamics · Lyapunov subcenter manifold · Reduced order modeling

1 Introduction

Nowadays, there is an ever-growing number of applications in which nonlinearities are exploited for functional purposes rather than avoided. These applications include frequency division (Qalandar et al. 2014), vibration mitigation (Bellet et al. 2010), nonlinear energy sinks, and targeted energy transfer (Vakakis et al. 2022). Other applications can be found in micromechanical sensors (Zhang et al. 2002; Marconi et al. 2021a).

Therefore, this increased interest in nonlinear dynamics has favored the development of different numerical methods in the field of reduced order models (ROM, Tiso et al. 2021; Touzé et al. 2021) to analyze and study the nonlinear dynamic behavior of mechanical systems. This behavior can be described through the nonlinear frequency–amplitude relation, which can be tracked by computing the *backbone curves* (see, e.g., Breunung and Haller 2018). Usually, these curves are obtained using numerical continuation techniques with the collocation method (Dankowicz and Schilder 2013), the Harmonic Balance Method (HBM, Krack and Gross 2019), or the shooting method (Kerschen et al. 2008). Alternatively, the *conservative backbone curves* can be computed using the reduced dynamics on Lyapunov Subcenter Manifolds (LS$\mathcal{M}$[1]), which has proven to be particularly effective for high-dimensional mechanical systems (Jain and Haller 2022).

However, despite all these techniques, controlling the nonlinear dynamic behavior of a system still remains a complex challenge. The main difficulty is identifying the

Responsible editor: Seonho Cho

✉ Jacopo Marconi
jacopo.marconi@polimi.it

[1] Department of Mechanical Engineering, Politecnico di Milano, Via G. La Masa, 1, Milan 20156, MI, Italy

[2] Delft Institute of Applied Mathematics, TU Delft, Mekelweg 4, Delft 2628CD, ZH, The Netherlands

[3] Department of Mechanics and Aerospace Engineering, Southern University of Science and Technology, Shenzhen, China

[1] We use LS$\mathcal{M}$ to distinguish the Lyapunov Subcenter Manifold from the LSM (Level Set Method), commonly used in topology optimization literature.

Published online: 24 April 2025

ideal set of parameters that will produce the desired frequency–amplitude relation. To address this issue, various optimization strategies have been proposed. For example, Schiwietz et al. (2024, 2025) used shape optimization to optimize the eigenfrequencies and the modal coupling coefficients of a geometrically nonlinear MEMS gyroscope, whereas Detroux et al. (2021) focused on tailoring backbone curves using nonlinear synthesis. Dou et al. (2015); Dou and Jensen (2015, 2016) developed methods to optimize hardening behaviors in resonators and plane frame structures via nonlinear normal modes (NNMs, Kerschen et al. 2009; Haller and Ponsioen 2016) and the HBM. Incidentally, we notice that in all these *parametric* optimization methods, the considered structures are of low dimension, usually featuring 2D beam elements and frame-like structures. However, computational times are usually omitted, making it challenging to assess their efficiency and scalability.

These optimization processes are highly sensitive to user-defined parameters, such as the number of harmonics in the harmonic balance method (HBM) or the arc-length parameter in numerical continuation, which may require adjustment during iterations due to changes in system behavior. Additionally, intrinsic limitations of the numerical method, particularly in HBM sensitivity analysis, may affect the optimization results (Saccani et al. 2022). One way to mitigate this issue is by employing alternative methods for computing the frequency–amplitude relation.

Recently, a parametric optimization approach was proposed to tailor the conservative backbone curve[2] of nonlinear mechanical systems by exploiting the reduced dynamics on the LS$\mathcal{M}$ (Pozzi et al. 2024). In that work, we highlighted several advantages of the LS$\mathcal{M}$'s analyticity in optimization, such as eliminating the need for user-defined parameters, simulations, or ROMs. However, the sensitivities are still computed via direct differentiation, which is computationally demanding as the number of optimization parameters increases.

Despite these advancements in nonlinear dynamics optimization, the available methods in the literature remain applicable only to small systems due to the high computational costs and limited scalability. As a result, topology optimization techniques (Bendsøe and Sigmund 2004), which involve a large number of design variables, are predominantly applied in the realm of *linear* structural dynamics (Silva et al. 2019; Li et al. 2021; Pozzi et al. 2023b), with applications extend to mechanical resonators (Yang and Li 2013, 2014; Pozzi et al. 2023a; Giannini et al. 2024), MEMS gyroscopes (Giannini et al. 2020, 2022), and piezoelectric energy harvesters (Townsend et al. 2019).

As previously discussed, nonlinear dynamic topology optimization is extremely resource-intensive. To address this challenge, studies such as those by Kim and Park (2010); Lee and Park (2015); Lu et al. (2021) have employed the Equivalent Static Load method (ESL, Choi and Park 2002). This approach converts the nonlinear dynamic problem into a linear static problem. Following a different approach, Dalklint et al. (2020) introduced a topology optimization method for finite-strain hyperelastic structures, incorporating lower bound constraints on the nonlinear eigenfrequencies. These eigenfrequencies are evaluated around the equilibrium configuration, which is determined by solving a nonlinear stationary problem. Similarly, Li et al. (2022) proposed an eigenvalue topology optimization problem with frequency-dependent material properties.

However, despite these attempts, there are no topology optimization approaches that *directly* target the *backbone curve* of nonlinear mechanical systems.

Our contribution

As a first step to this end, we focus on the third-order backbone coefficient, which governs the hardening or softening behavior of mechanical systems. As shown in Pozzi et al. (2024), the most resource-intensive part of this process is the sensitivity analysis. Recently, Li (2024) explicitly derived the sensitivities of third-order spectral submanifolds in mechanical systems using both the direct approach and the adjoint method. As pointed out by Li (2024), the computational performance of sensitivity via adjoint method highly depends on the efficiency of evaluating nonlinearities. Here, we follow the adjoint method as in Li (2024) but utilize the tensor notation (Marconi et al. 2020) to handle nonlinear terms more efficiently. This leads to a more efficient sensitivity expression and enables us to apply standard topology optimization algorithms. We use a density-based approach with the solid isotropic material with penalization scheme (SIMP, Bendsøe and Sigmund 1999). Nonetheless, the sensitivity formulation is also valid for other topology optimization approaches, e.g., the level set method (Wang et al. 2003; Allaire et al. 2004), evolutionary structural optimization (ESO) method (Xie and Steven 1993), and moving morphable components (MMC) method (Guo et al. 2014).

The remainder of the paper is organized as follows. In Sect. 2, we show how to compute the third-order backbone coefficient, denoted by γ, using the normal-form parametrization of the Lyapunov subcenter manifold. The sensitivity expressions of γ are derived in Sect. 3 using the adjoint method. In Sect. 4, we briefly discuss the topology optimization approach that is used to obtain the numerical examples in Sect. 5. Finally, we close with the conclusions in Sect. 6.

[2] For practical applications, conservative backbone curves rigorously approximate the backbones for lightly damped systems.

2 Mechanical system

2.1 General settings

Consider the following equation of motion for a generic autonomous, undamped, nonlinear mechanical system:

$$\mathbf{M}\ddot{\boldsymbol{x}} + \mathbf{K}\boldsymbol{x} + \boldsymbol{f}(\boldsymbol{x}) = \mathbf{0}, \tag{1}$$

where $\boldsymbol{x} \in \mathbb{R}^n$ is the displacement vector, n is the number of degrees of freedom, $\mathbf{M}, \mathbf{K} \in \mathbb{R}^{n \times n}$ are the mass and linear stiffness matrices, respectively, and $\boldsymbol{f}(\boldsymbol{x}) \in \mathbb{R}^n$ is a displacement-dependent nonlinear term. When considering geometric nonlinearities, in several cases (e.g., for continuum finite elements with linear elastic constitutive law and total Lagrangian formulation), this term can be exactly represented by

$$\boldsymbol{f}(\boldsymbol{x}) = \boldsymbol{f}_2(\boldsymbol{x}, \boldsymbol{x}) + \boldsymbol{f}_3(\boldsymbol{x}, \boldsymbol{x}, \boldsymbol{x}), \tag{2}$$

where $\boldsymbol{f}_2$ and $\boldsymbol{f}_3$ are the quadratic and cubic polynomial terms in the displacements, respectively, representing the internal nonlinear elastic forces.

The linear normal modes (LNM) of the system in Eq. (1) are obtained by solving the generalized eigenvalue problem

$$\left(-\omega^2 \mathbf{M} + \mathbf{K}\right)\boldsymbol{\varphi} = \mathbf{0}, \tag{3}$$

where ω and $\boldsymbol{\varphi}$ are the eigenfrequency and the eigenvector, respectively, associated with a given LNM, mass normalized as

$$\boldsymbol{\varphi}^T \mathbf{M} \boldsymbol{\varphi} = 1. \tag{4}$$

In the absence of nonlinearities, the term $\boldsymbol{f}(\boldsymbol{x})$ vanishes, and the system in Eq. (1) becomes linear. In this case, it is well known that a subset of LNM can rigorously describe the dynamics of the system. Indeed, this LNM subset spans an *invariant* subspace-a lower-dimensional space where any motion that starts within it remains confined to it at all times. Due to this invariance, LNMs provide a basis for *modal truncation*, a rigorous model order reduction method for linear systems. If we restrict the analysis to a single mode $\boldsymbol{\varphi}$, such a subspace takes the form of a (hyper-)plane, spanned by the two eigenvectors of the first-order system associated with that mode.

In nonlinear systems, and under certain conditions (see Kelley 1969), such a plane can be smoothly extended to an invariant manifold, which is a (hyper-)surface, filled with periodic orbits of the full system and tangent at the origin to the aforementioned plane. A schematic representation of these two constructs is provided in Fig. 1, where it is evident that the linear subspace and the manifold are almost indistinguishable for displacements small enough, but they considerably differ as we depart from the origin. In recent years, the theory of spectral submanifolds (SSMs) has emerged as a rigorous method to identify these manifolds for dissipative mechanical systems and utilize them for model order reduction of nonlinear oscillatory systems. In the conservative and autonomous limit, SSMs coincide with the so-called Lyapunov subcenter manifold (LS$\mathcal{M}$), a unique, analytic, two-dimensional nonlinear extension of the corresponding linear subspace.

As discussed in the following, the reduced dynamics on an LS$\mathcal{M}$ provides an analytic expression for the backbone curve of the corresponding mode. This analytic expression can then be used to derive explicit sensitivities for the optimization problem (Pozzi et al. 2024).

2.2 Model order reduction

We provide here a brief overview of the main steps in model order reduction using invariant manifolds, without discussing the underlying theory in detail. For a

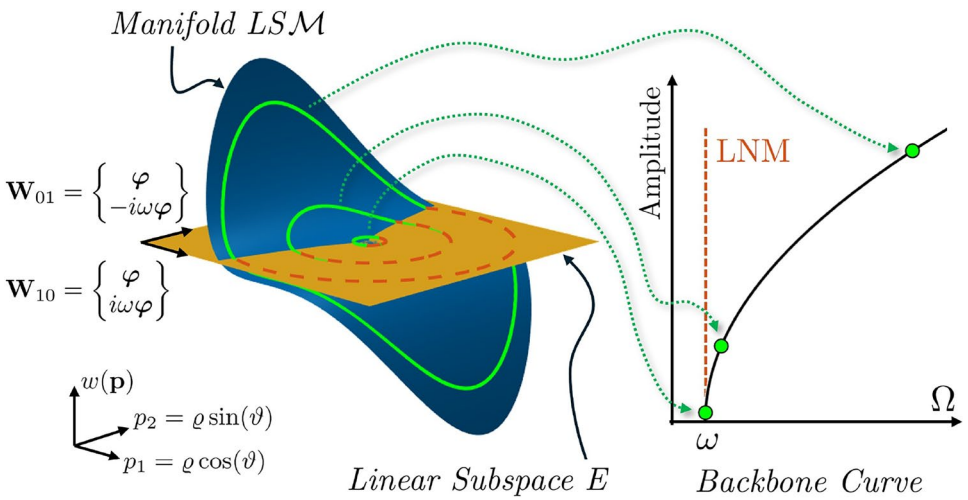

Fig. 1 Left: schematic representation of an invariant linear subspace E (yellow plane, spanned by the eigenvectors $\boldsymbol{W}_{01}$ and $\boldsymbol{W}_{10}$) and an invariant manifold tangent to it (blue surface). The conservative periodic orbits of the linear autonomous system lying on the linear subspace are drawn in red (dashed line), while the ones of the nonlinear system lying on the manifold are shown in green (solid line). Right: orbit amplitudes and frequencies construct the conservative backbone curve. The LNM is shown for completeness

comprehensive explanation, refer for instance to Jain and Haller (2022); Thurnher et al. (2024).

Let us assume that the reduced dynamics of a particular mode $\boldsymbol{\varphi}$ of the second-order system in Eq. (1) can be described by $M = 2$ reduced coordinates, collected in a vector $\boldsymbol{p} = \{p_1, p_2\}^T$. In a linear system, this would correspond to the vector of modal coordinates associated with the same mode (in first-order form), and the linear reduced dynamics would write as

$$\dot{\boldsymbol{p}} = \begin{bmatrix} i\omega & 0 \\ 0 & -i\omega \end{bmatrix} \boldsymbol{p}.$$

A similar approach can be sought for nonlinear systems using, among other methods, the *normal-form parametrization*. Letting $\boldsymbol{R} : \mathbb{C}^2 \to \mathbb{C}^2$ be a parametrization of the reduced dynamics, we can thus write:

$$\dot{\boldsymbol{p}} = \boldsymbol{R}(\boldsymbol{p}). \tag{5}$$

In linear systems, one would retrieve the full state of the system $\boldsymbol{z} = \{\boldsymbol{x}, \dot{\boldsymbol{x}}\}^T$ as $\boldsymbol{z} \approx \boldsymbol{W}\boldsymbol{p}$, where $\boldsymbol{W} = [\boldsymbol{W}_{01}, \boldsymbol{W}_{10}] \in \mathbb{R}^{2n\times 2}$ is a matrix collecting the two eigenvectors (see Fig. 1). Similarly, we can retrieve the full displacement of a conservative, autonomous nonlinear system by mapping the reduced coordinates to the LS$\mathcal{M}$.

Let $\boldsymbol{w} : \mathbb{C}^2 \to \mathbb{R}^n$ be a parametrization of the Lyapunov subcenter manifold around a (linear) master subspace E. We can write

$$\boldsymbol{x} = \boldsymbol{w}(\boldsymbol{p}), \tag{6}$$

being $\boldsymbol{w}(\boldsymbol{p})$ graphically represented as the blue surface in Fig. 1.

Finally, to numerically compute an approximation to $\boldsymbol{w}(\boldsymbol{p})$ and $\boldsymbol{R}(\boldsymbol{p})$, and adopting the multi-index notation, we can Taylor-expand them as

$$\boldsymbol{R}(\boldsymbol{p}) \approx \sum_{\boldsymbol{m}\in\mathbb{N}^2} \boldsymbol{R}_{\boldsymbol{m}} \boldsymbol{p}^{\boldsymbol{m}}, \tag{7a}$$

$$\boldsymbol{w}(\boldsymbol{p}) \approx \sum_{\boldsymbol{m}\in\mathbb{N}^2} \boldsymbol{w}_{\boldsymbol{m}} \boldsymbol{p}^{\boldsymbol{m}}, \tag{7b}$$

where $\boldsymbol{R}_{\boldsymbol{m}} \in \mathbb{C}^2$ and $\boldsymbol{w}_{\boldsymbol{m}} \in \mathbb{C}^n$ are the reduced dynamics and the manifold coefficients, respectively.

Finally, substituting Eqs. () into Eq. (1), one can solve for the coefficients $\boldsymbol{w}_{\boldsymbol{m}}$ and $\boldsymbol{R}_{\boldsymbol{m}}$. The procedure to compute them up to the third order is detailed in Appendix A (in particular, see Table 6).

2.3 Backbone curve

Transforming the reduced coordinates into polar notation as $\boldsymbol{p} = \varrho\{e^{i\vartheta}, e^{-i\vartheta}\}^T$, and after some manipulation, it can be shown that the following nonlinear frequency–amplitude relation holds:

$$\Omega = \omega + \sum_{m=2}^{m_{\max}} \gamma_m \varrho^{m-1}, \tag{8}$$

where Ω is the frequency of the response, ϱ is the amplitude in the reduced space, and γ_m are the coefficients of the backbone curve that come from the normal-form parametrization of the Lyapunov subcenter manifold. In particular, if the maximum expansion order is $m_{\max} = 3$, the backbone curve becomes

$$\Omega = \omega + \gamma_3 \varrho^2, \tag{9}$$

where γ_3 is the third-order backbone coefficient obtained from the reduced coefficient $\boldsymbol{R}_{\boldsymbol{m}}$ at order 3 (i.e., for $|\boldsymbol{m}|_1 = 3$).

In this case, the parameter γ_3, hereafter renamed γ to ease the notation, controls the hardening/softening behavior of the system (Fig. 2, de la Llave and Kogelbauer 2019) and reads (Li 2024):

$$\gamma = \frac{1}{2\omega} \boldsymbol{\varphi}^T \boldsymbol{f}_{21}. \tag{10}$$

In the following, only the relevant steps involved in the adjoint sensitivity analysis are reported (refer to Appendix C for more details).

The third-order nonlinear force associated with the multi-index $\boldsymbol{m} = \{2, 1\}$ is

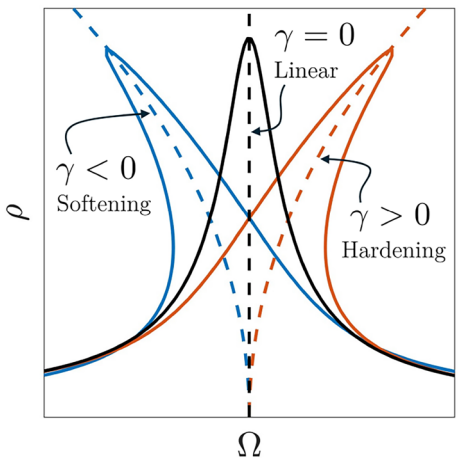

Fig. 2 Examples of backbone curves (dashed lines) of the autonomous, conservative systems and of the corresponding frequency response curves (solid lines) for their non-autonomous, non-conservative counterparts, where light damping has been considered

$$\begin{aligned} \boldsymbol{f}_{21} = &\boldsymbol{f}_2(\boldsymbol{w}_{20}, \boldsymbol{w}_{01}) + \boldsymbol{f}_2(\boldsymbol{w}_{01}, \boldsymbol{w}_{20}) \\ &+ \boldsymbol{f}_2(\boldsymbol{w}_{11}, \boldsymbol{w}_{10}) + \boldsymbol{f}_2(\boldsymbol{w}_{10}, \boldsymbol{w}_{11}) \\ &+ \boldsymbol{f}_3(\boldsymbol{w}_{10}, \boldsymbol{w}_{10}, \boldsymbol{w}_{01}) \\ &+ \boldsymbol{f}_3(\boldsymbol{w}_{10}, \boldsymbol{w}_{01}, \boldsymbol{w}_{10}) \\ &+ \boldsymbol{f}_3(\boldsymbol{w}_{01}, \boldsymbol{w}_{10}, \boldsymbol{w}_{10}). \end{aligned} \tag{11}$$

The vector $\boldsymbol{f}_{21}$ depends on the LS$\mathcal{M}$ coefficients at lower orders $\boldsymbol{w}_{20}$, $\boldsymbol{w}_{11}$, $\boldsymbol{w}_{10}$, and $\boldsymbol{w}_{01}$. These can be computed using the set of equations listed below:

$$\boldsymbol{f}_{20} = \boldsymbol{f}_2(\boldsymbol{w}_{10}, \boldsymbol{w}_{10}), \tag{12a}$$

$$\mathbf{L}_{20} = \mathbf{K} + \Lambda_{20}^2 \mathbf{M} = \mathbf{K} - 4\omega^2 \mathbf{M}, \tag{12b}$$

$$\mathbf{L}_{20}\boldsymbol{w}_{20} + \boldsymbol{f}_{20} = \mathbf{0}, \tag{12c}$$

and

$$\boldsymbol{f}_{11} = \boldsymbol{f}_2(\boldsymbol{w}_{10}, \boldsymbol{w}_{01}) + \boldsymbol{f}_2(\boldsymbol{w}_{01}, \boldsymbol{w}_{10}), \tag{13a}$$

$$\mathbf{L}_{11} = \mathbf{K} + \Lambda_{11}^2 \mathbf{M} = \mathbf{K}, \tag{13b}$$

$$\mathbf{L}_{11}\boldsymbol{w}_{11} + \boldsymbol{f}_{11} = \mathbf{0}, \tag{13c}$$

and

$$\boldsymbol{w}_{10} = \boldsymbol{w}_{01} = \boldsymbol{\varphi}. \tag{14}$$

Remark (On generalization). The results recalled in this section hold for an autonomous, conservative *second-order* nonlinear system of ODEs. However, LS$\mathcal{M}$ (and SSM, de la Llave and Kogelbauer 2019) theory holds for generic first-order nonlinear systems of ODEs, therefore extensions to other problems and physical domains are also possible.

3 Adjoint sensitivity analysis

When dealing with optimization problems with a large number of design variables, e.g., topology optimization, the sensitivities are usually obtained using the adjoint method. For instance, provided that the mode shape $\boldsymbol{\varphi}$ is mass normalized (Eq. (4), the sensitivity of the eigenfrequency ω (Bendsøe and Sigmund 2004) is computed as

$$\frac{\mathrm{d}\omega}{\mathrm{d}\mu} = \frac{\boldsymbol{\varphi}^T \left(\frac{\partial \mathbf{K}}{\partial \mu} - \omega^2 \frac{\partial \mathbf{M}}{\partial \mu} \right) \boldsymbol{\varphi}}{2\omega}. \tag{15}$$

Using the same approach, the sensitivity of γ is computed using the adjoint method. We follow the derivation in Li (2024) but restrict to the case of undamped system. The *state variables* of this problem are $\boldsymbol{\varphi}$, ω, $\boldsymbol{w}_{20}$, and $\boldsymbol{w}_{11}$. Each of them is associated with a *state function* (Eqs. (3), (4), (12), and (13)) and with an *adjoint variable* (λ_0, λ_1, λ_{20}, and λ_{11}). Using this terms, the Lagrangian function $\mathcal{L}$ is defined as follows:

$$\begin{aligned} \mathcal{L} = &\gamma + \lambda_0^T (\mathbf{K} - \omega^2 \mathbf{M}) \boldsymbol{\varphi} \\ &+ \lambda_1 (\boldsymbol{\varphi}^T \mathbf{M} \boldsymbol{\varphi} - 1) \\ &+ \lambda_{20}^T (\mathbf{L}_{20} \boldsymbol{w}_{20} + \boldsymbol{f}_{20}) \\ &+ \lambda_{11}^T (\mathbf{L}_{11} \boldsymbol{w}_{11} + \boldsymbol{f}_{11}). \end{aligned} \tag{16}$$

The *adjoint variables* are computed by solving the *adjoint equations*, which are obtained by differentiating $\mathcal{L}$ with respect to the *state variables*:

$$\frac{\partial \mathcal{L}}{\partial \boldsymbol{w}_{20}} = \frac{\partial \gamma}{\partial \boldsymbol{w}_{20}} + \lambda_{20} \mathbf{L}_{20} = \mathbf{0}^T \tag{17}$$

$$\frac{\partial \mathcal{L}}{\partial \boldsymbol{w}_{11}} = \frac{\partial \gamma}{\partial \boldsymbol{w}_{11}} + \lambda_{11} \mathbf{L}_{11} = \mathbf{0}^T \tag{18}$$

$$\begin{aligned} \frac{\partial \mathcal{L}}{\partial \boldsymbol{\varphi}} = &\frac{\partial \gamma}{\partial \boldsymbol{\varphi}} + \lambda_0^T (\mathbf{K} - \omega^2 \mathbf{M}) \\ &+ 2\lambda_1 \boldsymbol{\varphi}^T \mathbf{M} + \lambda_{20}^T \frac{\partial \boldsymbol{f}_{20}}{\partial \boldsymbol{\varphi}} \\ &+ \lambda_{11}^T \frac{\partial \boldsymbol{f}_{11}}{\partial \boldsymbol{\varphi}} = \mathbf{0}^T \end{aligned} \tag{19}$$

$$\begin{aligned} \frac{\partial \mathcal{L}}{\partial \omega} = &\frac{\partial \gamma}{\partial \omega} - 2\omega \lambda_0^T \mathbf{M} \boldsymbol{\varphi} \\ &- 8\omega \lambda_{20}^T \mathbf{M} \boldsymbol{w}_{20} = 0. \end{aligned} \tag{20}$$

Equations (19) and (20) are solved together by creating the system

$$\begin{bmatrix} \mathbf{K} - \omega^2 \mathbf{M} & 2\mathbf{M}\boldsymbol{\varphi} \\ 2\boldsymbol{\varphi}^T \mathbf{M} & 0 \end{bmatrix} \begin{bmatrix} \lambda_0 \\ \lambda_1 \end{bmatrix} = \begin{bmatrix} \boldsymbol{b}_{\boldsymbol{\varphi}} \\ b_\omega \end{bmatrix}, \tag{21}$$

where the terms in the right-hand side are defined as

$$\boldsymbol{b}_{\boldsymbol{\varphi}}^T = -\frac{\partial \gamma}{\partial \boldsymbol{\varphi}} - \lambda_{20}^T \frac{\partial \boldsymbol{f}_{20}}{\partial \boldsymbol{\varphi}} - \lambda_{11}^T \frac{\partial \boldsymbol{f}_{11}}{\partial \boldsymbol{\varphi}} \tag{22a}$$

$$b_\omega = \frac{1}{\omega} \left(\frac{\partial \gamma}{\partial \omega} - 8\omega \lambda_{20}^T \mathbf{M} \boldsymbol{w}_{20} \right). \tag{22b}$$

Finally, the sensitivity of γ is equal to the partial derivative of $\mathcal{L}$ with respect to the design variables μ:

$$\begin{aligned}\frac{\mathrm{d}\gamma}{\mathrm{d}\mu} &= \frac{\partial \mathcal{L}}{\partial \mu} \\ &= \frac{\partial \gamma}{\partial \mu} + \boldsymbol{\lambda}_0^T \left(\frac{\partial \mathbf{K}}{\partial \mu} - \omega^2 \frac{\partial \mathbf{M}}{\partial \mu} \right) \boldsymbol{\varphi} \\ &\quad + \lambda_1 \boldsymbol{\varphi}^T \frac{\partial \mathbf{M}}{\partial \mu} \boldsymbol{\varphi} \\ &\quad + \boldsymbol{\lambda}_{20}^T \left(\frac{\partial \mathbf{L}_{20}}{\partial \mu} \boldsymbol{w}_{20} + \frac{\partial \boldsymbol{f}_{20}}{\partial \mu} \right) \\ &\quad + \boldsymbol{\lambda}_{11}^T \left(\frac{\partial \mathbf{L}_{11}}{\partial \mu} \boldsymbol{w}_{11} + \frac{\partial \boldsymbol{f}_{11}}{\partial \mu} \right),\end{aligned} \tag{23}$$

where the partial derivatives of the matrices and vectors $\mathbf{K}$, $\mathbf{M}$, and $\boldsymbol{f}$ depend on the formulation of the mechanical system under consideration. Notice that $\partial\gamma/\partial\mu = 0$. This formula is consistent with equation (111) of Li (2024) when damping coefficients α and β in (111) are set to be zero.

All the details on the partial derivatives are given in Appendix C.

The sensitivity expression in Eq. (23) is validated against finite differences perturbing 50 randomly selected elements over the grid used in Sect. 5.1, with different steps $\delta\mu$:

$$\frac{\mathrm{d}\gamma(\mu)}{\mathrm{d}\mu} \approx \frac{\gamma(\mu) - \gamma(\mu - \delta\mu)}{\delta\mu}. \tag{24}$$

The small magnitude of the relative error (Fig. 3) confirms the validity of the adjoint method implementation.

4 Topology optimization algorithm

In this work, the density-based topology optimization approach is used with the solid isotropic material with penalization (SIMP, Bendsøe and Sigmund 1999) interpolation scheme. As mentioned in the introduction, any topology optimization method can be chosen, and the SIMP choice is dictated only by the ease of implementation in YetAnotherFEcode (Jain et al. 2022). In any case, according to the numerical tests that will be discussed in Sect. 5, topology optimization routines account only for approximately the 4% of the whole iteration computational time. The design domain is discretized using a structured grid made of bilinear squared elements, each one is characterized by density μ (Fig. 4).

To obtain a well-posed optimization problem, to avoid mesh dependent solutions, and to prevent gray transition regions, the regularization filter described in Wang et al. (2011) is used:

$$\tilde{\mu}_e = \frac{\sum_{j \in \mathcal{N}_e} w_{j,e} \mu_j}{\sum_{j \in \mathcal{N}_e} w_{j,e}}, \tag{25}$$

where $\tilde{\mu}_e$ is the filtered density of the element e, $\mathcal{N}_e$ is a set that contains the indices of the elements that lay within a circle of radius R around element e, and $w_{j,e}$ is a weight defined as

$$w_{j,e} = R - |\boldsymbol{x}_j - \boldsymbol{x}_e|, \tag{26}$$

where $\boldsymbol{x}_e$ and $\boldsymbol{x}_j$ are the coordinates of the centroids of elements e and j. In this work, $R = 4$ is used.

The filtered densities are then projected through the projection threshold presented in Wang et al. (2011):

$$\bar{\mu}_e = \frac{\tanh(\beta\eta) + \tanh(\beta(\tilde{\mu}_e - \eta))}{\tanh(\beta\eta) + \tanh(\beta(1 - \eta))}, \tag{27}$$

where $\bar{\mu}_e$ is the projected density of element e, and β and η are projection parameters. In this work, $\beta = 10$ and $\eta = 0.5$ are selected.

Finally, the SIMP scheme is used to obtain the physical densities $\hat{\mu}$ from the projected ones $\bar{\mu}$:

$$\hat{\mu}_e = \hat{\mu}_0 + (1 - \hat{\mu}_0)\bar{\mu}_e^p, \tag{28}$$

where p is the penalization power, and $\hat{\mu}_0$ is an arbitrary small density of the void element, used to prevent singularities in the numerical method. To ensure a 0/1 design, $\hat{\mu}_0 = 10^{-6}$ is

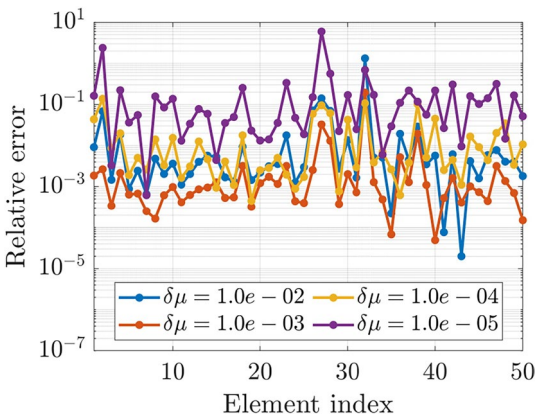

Fig. 3 Validation of the sensitivity of γ (Eq. (23)) using finite differences

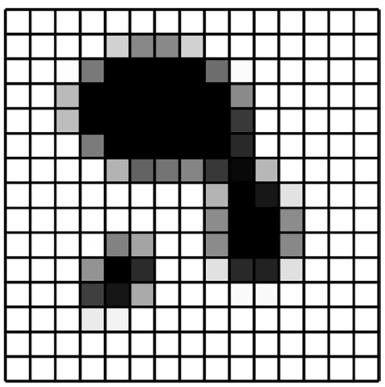

Fig. 4 Example of structure discretization using element densities

used and p is gradually increased during the optimization starting from 1.

The physical densities $\hat{\mu}$ are then used to interpolate the material properties:

$$\mathbf{M} = \bigcup_{e=1}^{N_{\text{el}}} \hat{\mu}_e \mathbf{M}_e, \tag{29a}$$

$$\mathbf{K} = \bigcup_{e=1}^{N_{\text{el}}} \hat{\mu}_e \mathbf{K}_e, \tag{29b}$$

$$F_2 = \bigcup_{e=1}^{N_{\text{el}}} \hat{\mu}_e F_{2e}, \tag{29c}$$

$$F_3 = \bigcup_{e=1}^{N_{\text{el}}} \hat{\mu}_e F_{3e}, \tag{29d}$$

where N_{el} is the total number of elements, $F_2 \in \mathbb{R}^{n\times n\times n}$ and $F_3 \in \mathbb{R}^{n\times n\times n\times n}$ are the quadratic and cubic stiffness tensors, and where we use the subscript e to denote the same entities at element level. The operator $\bigcup$ represents the finite element assembly across all the elements of the grid. Since a structured grid is used, *the element matrices and tensors are the same for all the elements*. Therefore, they can be computed only once and for all, considerably alleviating the total computational cost.

Remark (Nonintrusive implementation). The presented approach employs tensors that are not commonly available in standard FE codes. However, non-intrusive techniques can be used to evaluate nonlinear forces, as demonstrated by Li et al. (2025). While this circumvents the need for tensors, it comes at the cost of losing the previously mentioned advantages. Specifically, in this case, the regularity of the mesh cannot be exploited, as each term would depend on the displacement vector $\boldsymbol{x}$, requiring evaluations to be carried out for every individual element over the entire mesh.

To compute adjoint sensitivities (Eqs. (15) and (23)), partial derivatives of $\mathbf{M}$, $\mathbf{K}$, F_2 , and F_3 are required with respect to μ. This partial derivatives involve differentiating Eqs. (25), (27), and (28). The detailed expressions for these derivatives are provided in Appendix D.

5 Numerical examples

In this section, numerical examples are presented to show the validity of the adjoint sensitivity formulation. In all the examples, the 2-dimensional design domain is discretized using a structured grid made of 4-node, square elements with bilinear shape functions. The material considered is polysilicon (Acar and Shkel 2009), which is characterized by density 2330 kg/m^3, Young's modulus 148 GPa, and Poisson's coefficient 0.23. The plane stress approximation is used, with a thickness of 24 µm.

During the optimization, the modal assurance criterion (MAC, Kim and Kim 2000) is used to track the targeted mode, thus allowing to deal with mode switching and to neglect artificial modes that may arise (Pozzi et al. 2023a).

In particular, the MAC value is a measure of the similarity of two mode shapes:

$$\text{MAC}_{ij} = \frac{|\boldsymbol{\varphi}_i^T \boldsymbol{\varphi}_j|^2}{(\boldsymbol{\varphi}_i^T \boldsymbol{\varphi}_i)(\boldsymbol{\varphi}_j^T \boldsymbol{\varphi}_j)}. \tag{30}$$

At each iteration, the MAC is used to compare a set of modes with the shape of the target one. This target shape is either known *a priori* or selected at the first iteration. The mode shape with the highest MAC value is the target one.

The optimization problem is implemented in MATLAB R2023b using YetAnotherFEcode (Jain et al. 2022) and solved with the Method of Moving Asymptotes (MMA, Svanberg 1987).

The most expensive part of the optimization loop is the evaluation of γ and its sensitivity, accounting for around 96% of the total iteration time. Table 1 summarizes these computational times, measured on a Windows laptop with an Intel Core i7-1255U CPU @ 1.70 GHz and 16 GB of RAM @ 3200 MT/s, using different number of elements.

For each example, the optimal layout, the third-order backbone curve in the *reduced space* (Eq. (8)), and the third-order backbone curve in the *physical space* are shown. In particular, the latter is computed on the optimal layout using the SSMTool (Jain et al. 2023) at $\mathcal{O}(3)$ and $\mathcal{O}(7)$ expansion orders.

Remark (ROM accuracy). The presented optimization scheme focuses on γ, the lowest order nonlinearity coefficient appearing in the backbone curve expression of Eq. (8). As such, we can only guarantee that for a small enough displacement amplitude the dynamic behavior of the system will be of the hardening or softening type, quantitatively determined by the target value of γ. For high enough amplitudes, the

Table 1 Computational times for the evaluation of γ and its sensitivity, measured on a Windows laptop with an Intel Core i7-1255U CPU @ 1.70 GHz and 16 GB of RAM @ 3200 MT/s. These times also include the assembly of matrices and tensors, accounting for approximately half of the reported computational time

Grid	Elements	Time
100×20	2000	4.05
100×50	5000	10.29
100×100	10,000	20.29
200×100	20,000	41.51

third-order approximation is expected to become less accurate, as higher order terms in Eq. (8) may be required to describe the dynamics of the system.

5.1 MBB beam

The first example is the Messerschmitt-Bölkow-Blohm (MBB) beam with a fixed region (20 % of the total beam length) in the middle that acts like a proof mass. Thanks to design symmetries, only the left half of the beam is modeled (Fig. 5). The design domain (500 µm × 100 µm) is discretized using a 100 × 20 grid. A constraint on the maximum area fraction $A_{\max} = 50\,\%$ is used to limit the material usage.

Using these same settings and initial conditions, we set up 3 frequency maximization problems applying different constraints. In all cases, the target frequency ω corresponds to the mode shape featuring a vertical oscillation of the proof mass.

The total number of iterations, along with the computational times, for the three examples are reported in Table 3.

MBB—Linear Optimization

First, the following classic frequency maximization problem is solved, with no constraints on γ:

$$\begin{aligned} \max_{\mu} \quad & \omega \\ \text{s.t.} \quad & A \le A_{\max}. \end{aligned} \tag{31}$$

The optimal layout (left column of Fig. 6) is characterized by a positive γ, as indicated in Table 2. A positive γ corresponds to a material configuration that exhibits hardening behavior, where the structure's dynamic stiffness increases with increasing deformation.

MBB—softening optimization

A softening behavior can be obtained including a negative upper bound on the value of γ. To this end, the optimization problem is recast as

$$\begin{aligned} \max_{\mu} \quad & \omega \\ \text{s.t.} \quad & \gamma \le \gamma_{\max} \\ & A \le A_{\max}, \end{aligned} \tag{32}$$

Fig. 5 Problem settings and initial conditions for the MBB beam. Only the left half of the structure is optimized. The left side is fixed, while the right side can move vertically but not horizontally. A black region (20 % of the total beam length) is used as a proof mass

where a $\gamma_{\max} = -10^{-3}$ is used, reasonably selected by comparison with the outcome value of γ from the previous linear optimization.

The result (middle column of Fig. 6) is characterized by a negative value of γ, as indicated in Table 2, leading to the desired softening behavior. A negative γ implies that the structure undergoes a reduction in stiffness for increasing oscillation amplitudes. Interestingly, in this case, the optimization process converged to an asymmetric layout about the horizontal axis, exhibiting behavior similar to that of curved beams or arches (Marconi et al. 2021b).

MBB—hardening optimization

We now add a positive lower bound to the coefficient γ. The aim here is to control the hardening behavior of the structure. The optimization problem becomes

$$\begin{aligned} \max_{\mu} \quad & \omega \\ \text{s.t.} \quad & \gamma \ge \gamma_{\min} \\ & A \le A_{\max}, \end{aligned} \tag{33}$$

where $\gamma_{\min} = 10^{-3}$ is selected.

The optimal solution is presented in the right column of Fig. 6. This structure exhibits a positive γ, indicating the desired hardening behavior. In particular, the value of γ is an order of magnitude larger compared to the solution of Problem (31), showing a significantly enhanced stiffness response under deformation (Table 3).

5.2 Single mass MEMS resonator

The second example is a single mass MEMS resonator for high-frequency applications. The design domain (1000 µm × 500 µm) is discretized using a 200 × 100 grid. Problem settings and boundary conditions are described in Fig. 7. The black region represents the proof mass that remains constant for the entire optimization. Fixed boundary conditions are applied to both the left and right sides of the domain.

The first optimization problem aims at imposing the frequency ω_Y, which corresponds to the mode shape with the maximum displacement of the proof mass along the Y direction. To avoid material detachment and connectivity issues, a constraint (or the objective function) is chosen to maximize the frequency ω_X, which corresponds to the mode shape with the oscillations of the proof mass along the X direction. A constraint on the maximum allowable area is also applied. Again, using these common settings, the optimization is carried out for 3 different cases.

The total number of iterations, along with the computational times, for the three examples are reported in Table 5.

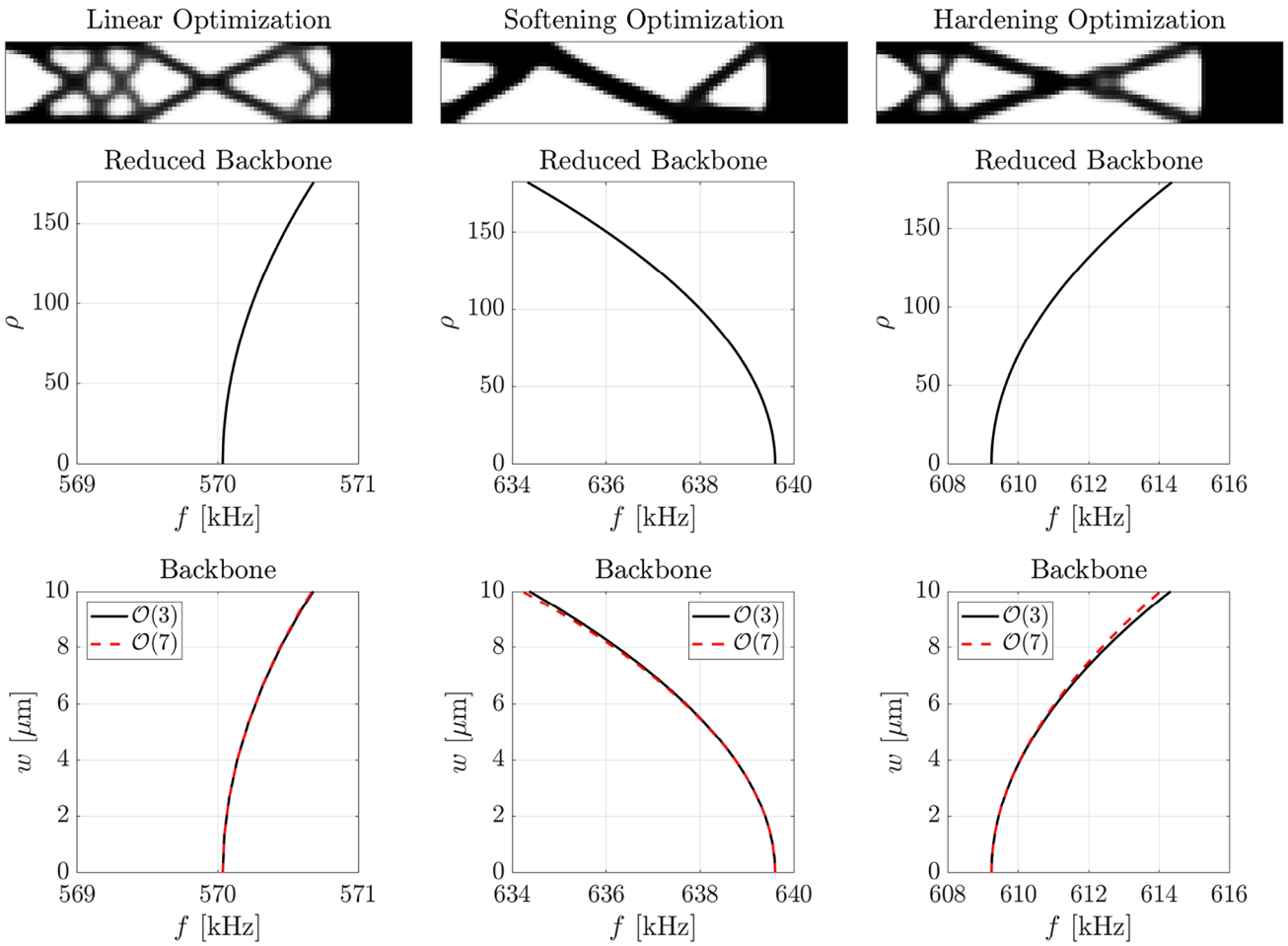

Fig. 6 Optimal results of the beam examples (Sect. 5.1). Left column: linear optimization (Problem (31)). Middle column: softening optimization (Problem (32)). Right column: hardening optimization (Problem (33)). The second row shows the third-order backbone curves in the reduced space (Eq.(8)), while the last row shows the backbone curves in the physical space using two different expansion orders

Table 2 Optimal results of the beam examples (Sect. 5.1)

Optimization	ω [kHz]	γ
Linear (31)	570.0	$1.3 \cdot 10^{-4}$
Softening (32)	639.6	$-1.0 \cdot 10^{-3}$
Hardening (33)	609.2	$1.0 \cdot 10^{-3}$

Table 3 Total iterations and computational times of the beam examples (Sect. 5.1), measured on a Windows laptop with an Intel Core i7-1255U CPU @ 1.70 GHz and 16 GB of RAM @ 3200 MT/s

Optimization	Iterations	Time
Linear (31)	180	21 s
Softening (32)	197	13 min 35 s
Hardening (33)	149	9 min 53 s

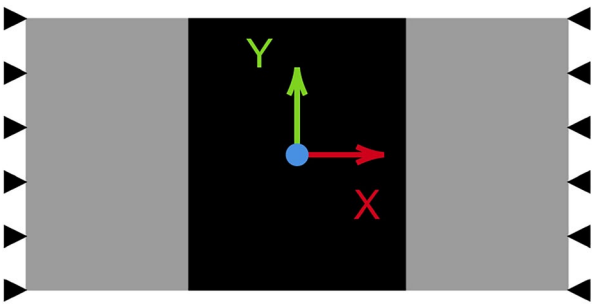

Fig. 7 Problem settings and initial conditions for the MEMS resonator

MEMS—linear optimization

The optimization problem is initially formulated without any particular constraint on γ and maximizing the objective function ω_X:

$$\begin{aligned} \max_{\boldsymbol{\mu}} \quad & \omega_X \\ \text{s.t.} \quad & (\omega_Y/\omega_{Y,\text{target}} - 1)^2 \leq \varepsilon^2 \\ & A \leq A_{\max}, \end{aligned} \tag{34}$$

where $A_{\max} = 60\,\%$ and $\omega_{Y,\text{target}} = 1000\,\text{kHz}$ is the target frequency value. The value of ε represents the relative error of ω_Y with respect to $\omega_{Y,\text{target}}$. For this problem, $\varepsilon = 10^{-2}$ is used, meaning that the constraints is satisfied if the value of ω_Y is within 10 % of the target value (between 990 kHz and 1010 kHz).

The optimal layout (left column of Fig. 8) is characterized by a small positive nonlinear coefficient associated with ω_Y. This results in an almost linear behavior in the considered oscillation amplitude range.

MEMS—softening optimization

Problem (34) is now modified to minimize the coefficient γ while imposing the same constraints on the target frequency ω_Y and the maximum allowed area. The maximization of ω_X (required to avoid material detachment and connectivity issues) is recast as an additional inequality constraint. The softening optimization problem reads:

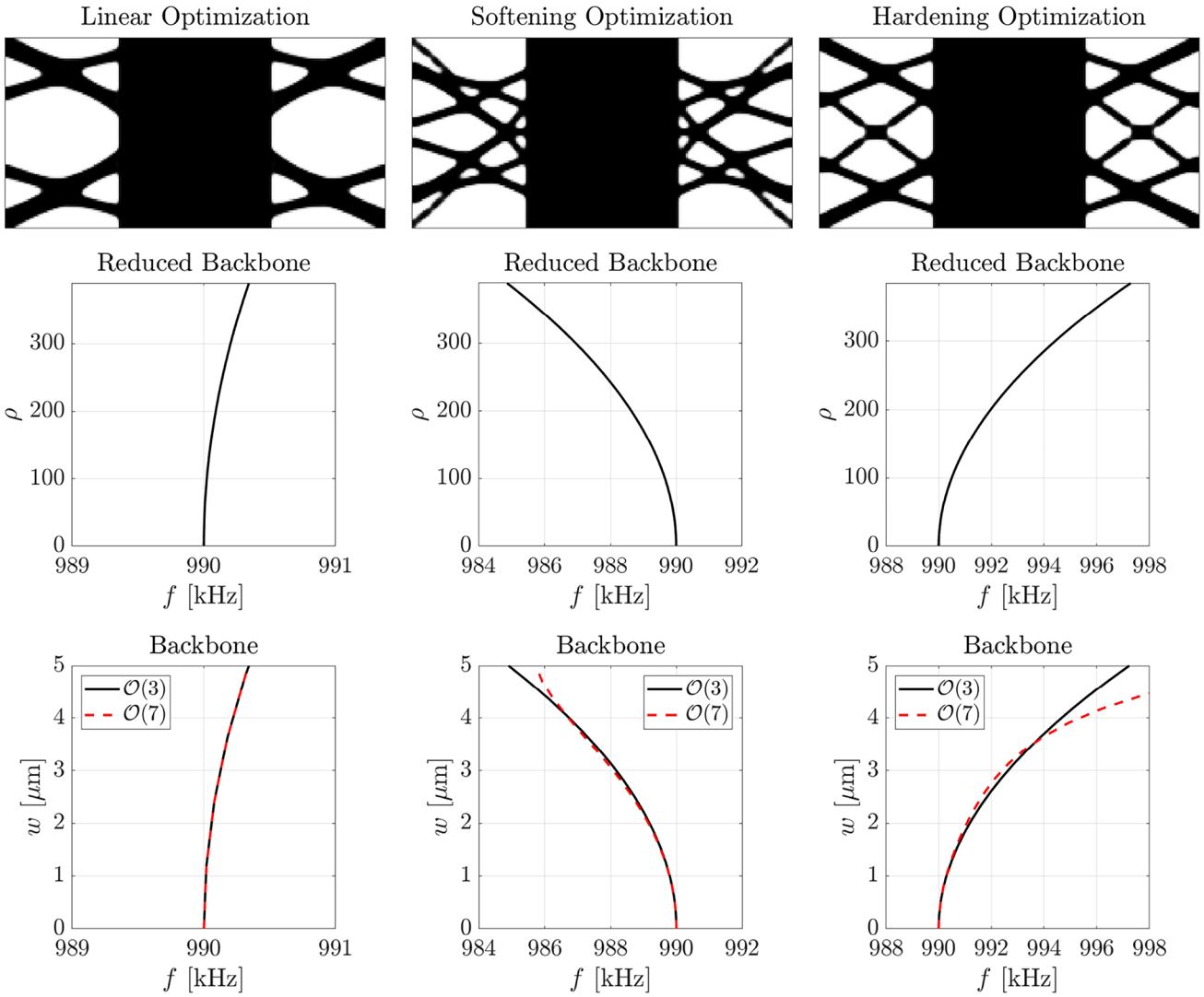

Fig. 8 Optimal results of the MEMS resonator examples (Sect. 5.2). Left column: results obtained solving Problem (34). Middle column: results obtained solving Problem (35). Right column: results obtained solving Problem (36). The second row shows the third-order backbone curves in the reduced space (Eq.(8)), while the last row shows the backbone curves in the physical space using two different expansion orders

Table 4 Optimal results of the MEMS resonator examples (Sect. 5.2)

Optimization	ω_Y [kHz]	ω_X [kHz]	γ
Linear (34)	990.0	2256	$1.4 \cdot 10^{-5}$
Softening (35)	990.0	2000	$-2.1 \cdot 10^{-4}$
Hardening (36)	990.0	2000	$3.1 \cdot 10^{-4}$

$$\begin{aligned} \min_{\boldsymbol{\mu}} \quad & \gamma \\ \text{s.t.} \quad & (\omega_Y/\omega_{Y,\text{target}} - 1)^2 \leq \varepsilon^2 \\ & \omega_X \geq \omega_{X,\min} \\ & A \leq A_{\max}, \end{aligned} \tag{35}$$

where $\omega_{X,\min} = 2000\,\text{kHz}$.

The result of the optimization (middle column of Fig. 8) is characterized by a negative value of γ, as indicated in Table 4, leading to the desired softening behavior.

MEMS—hardening optimization

Finally, Problem (35) is modified to maximize the coefficient γ:

$$\begin{aligned} \max_{\boldsymbol{\mu}} \quad & \gamma \\ \text{s.t.} \quad & (\omega_Y/\omega_{Y,\text{target}} - 1)^2 \leq \varepsilon^2 \\ & \omega_X \geq \omega_{X,\min} \\ & A \leq A_{\max}, \end{aligned} \tag{36}$$

where all the constraints are the same as in Problem (35).

The optimal solution is presented in the right column of Fig. 8. This structure exhibits a positive γ (Table 4), indicating the desired hardening behavior. In particular, the value of γ is an order of magnitude larger compared to the solution of Problem (34) (Table 5).

6 Conclusions

In this paper, we proposed a structural topology optimization method designed to tailor the hardening and softening dynamic behavior of nonlinear mechanical systems. The main advantage of the proposed approach is that it eliminates the need for costly full-order simulations or numerical continuation and significantly reduces the computational effort in optimizing the backbone curve. This reduction is achieved rigorously via analytical expressions for computing the conservative backbone from the reduced dynamics on the corresponding Lyapunov subcenter manifold.

We demonstrated how the integration of the adjoint method for the sensitivity analysis, combined with the tensor notation for expressing nonlinear internal forces, further enhances the computational efficiency of the proposed optimization process, especially for high-dimensional finite element models. The tensorial formulation not only simplifies sensitivity evaluations but, when applied to regular grids of elements, proves highly efficient in terms of computation. Numerical examples have been provided to show the validity of the proposed optimization.

Table 5 Total iterations and computational times of the MEMS resonator examples (Sect. 5.2), measured on a Windows laptop with an Intel Core i7-1255U CPU @ 1.70 GHz and 16 GB of RAM @ 3200 MT/s

Optimization	Iterations	Time
Linear (34)	141	4 min 16 s
Softening (35)	423	5 h 14 min 50 s
Hardening (36)	269	3 h 13 min 51 s

While the current work focuses on third-order expansions and on the coefficient γ, future extensions could adapt the approach to higher orders and to different optimization targets. Arbitrary order expansions would open up the possibility of adaptive algorithms to control the accuracy of the ROM during optimization, as done in Pozzi et al. (2024). Moreover, the adjoint formulation could be recast in order to optimize directly the backbone or the frequency response curves in the physical space. All these developments are currently underway (Pozzi et al. 2025).

Appendix A

Multi-index notation and $\mathcal{O}(3)$–LSM

A multi-index $\boldsymbol{m} \in \mathbb{N}^M$ of order $m = |\boldsymbol{m}|_1$ is an M-dimensional vector for which addition, subtraction, and other operations are defined element-wise. For instance, the multi-indices can be used to define multivariate monomials of order m as

$$\boldsymbol{p}^{\boldsymbol{m}} = p_1^{m_1} \cdots p_M^{m_M}. \tag{A1}$$

To denote quantities related to a specific multi-index $\boldsymbol{m} = \{x, y\}$, we use the subscript $\bullet_{xy}$. For instance, the parametrization coefficient related to $\boldsymbol{m} = \{2, 1\}$ is $\boldsymbol{R}_{21}$.

In this work, the two parametrizations (Eqs. (5) and (6)) are expanded up to the third order. As summarized in Table 6, $\boldsymbol{w}_{\boldsymbol{m}}$ and $\boldsymbol{R}_{\boldsymbol{m}}$ are computed sequentially, starting from the first order ($|\boldsymbol{m}|_1 = 1$). More details can be found in Li (2024).

Table 6 Lyapunov subcenter manifold computations at leading, second, and third order

	$\boldsymbol{m}=\{1,0\}$	$\boldsymbol{m}=\{0,1\}$		
$\lvert\boldsymbol{m}\rvert_1$=1	$\boldsymbol{w}_{10}=\boldsymbol{\varphi}$ $\boldsymbol{R}_{10}=\begin{bmatrix}\mathrm{i}\omega\\0\end{bmatrix}$	$\boldsymbol{w}_{01}=\boldsymbol{\varphi}$ $\boldsymbol{R}_{01}=\begin{bmatrix}0\\-\mathrm{i}\omega\end{bmatrix}$		
	$\boldsymbol{m}=\{2,0\}$	$\boldsymbol{m}=\{1,1\}$	$\boldsymbol{m}=\{0,2\}$	
$\lvert\boldsymbol{m}\rvert_1$=2	$\boldsymbol{f}_{20}=\boldsymbol{f}_2(\boldsymbol{w}_{10},\boldsymbol{w}_{10})$ $\boldsymbol{R}_{20}=\mathbf{0}$ $\Lambda_{20}=\mathrm{i}2\omega$ $\mathbf{L}_{20}=\mathbf{K}+\Lambda_{20}^2\mathbf{M}$ $\mathbf{L}_{20}\boldsymbol{w}_{20}+\boldsymbol{f}_{20}=\mathbf{0}$	$\boldsymbol{f}_{11}=\boldsymbol{f}_2(\boldsymbol{w}_{10},\boldsymbol{w}_{01})$ $\quad+\boldsymbol{f}_2(\boldsymbol{w}_{01},\boldsymbol{w}_{10})$ $\boldsymbol{R}_{11}=\mathbf{0}$ $\Lambda_{11}=0$ $\mathbf{L}_{11}=\mathbf{K}+\Lambda_{11}^2\mathbf{M}=\mathbf{K}$ $\mathbf{L}_{11}\boldsymbol{w}_{11}+\boldsymbol{f}_{11}=\mathbf{0}$	$\boldsymbol{f}_{02}=\boldsymbol{f}_2(\boldsymbol{w}_{01},\boldsymbol{w}_{01})$ $\boldsymbol{R}_{02}=\mathbf{0}$ $\Lambda_{02}=-\mathrm{i}2\omega$ $\mathbf{L}_{02}=\mathbf{K}+\Lambda_{02}^2\mathbf{M}$ $\mathbf{L}_{02}\boldsymbol{w}_{02}+\boldsymbol{f}_{02}=\mathbf{0}$	
	$\boldsymbol{m}=\{3,0\}$	$\boldsymbol{m}=\{2,1\}$	$\boldsymbol{m}=\{1,2\}$	$\boldsymbol{m}=\{0,3\}$
$\lvert\boldsymbol{m}\rvert_1$=3	$\boldsymbol{f}_{30}=\boldsymbol{f}_2(\boldsymbol{w}_{20},\boldsymbol{w}_{10})$ $\quad+\boldsymbol{f}_2(\boldsymbol{w}_{10},\boldsymbol{w}_{20})$ $\quad+\boldsymbol{f}_3(\boldsymbol{w}_{10},\boldsymbol{w}_{10},\boldsymbol{w}_{10})$ $\boldsymbol{R}_{30}=\mathbf{0}$ $\Lambda_{30}=\mathrm{i}3\omega$ $\mathbf{L}_{30}=\mathbf{K}+\Lambda_{30}^2\mathbf{M}$ $\mathbf{L}_{30}\boldsymbol{w}_{30}+\boldsymbol{f}_{30}=\mathbf{0}$	$\boldsymbol{f}_{21}=\boldsymbol{f}_2(\boldsymbol{w}_{10},\boldsymbol{w}_{11})$ $\quad+\boldsymbol{f}_2(\boldsymbol{w}_{11},\boldsymbol{w}_{10})$ $\quad+\boldsymbol{f}_2(\boldsymbol{w}_{01},\boldsymbol{w}_{20})$ $\quad+\boldsymbol{f}_2(\boldsymbol{w}_{20},\boldsymbol{w}_{01})$ $\quad+\boldsymbol{f}_3(\boldsymbol{w}_{10},\boldsymbol{w}_{10},\boldsymbol{w}_{01})$ $\quad+\boldsymbol{f}_3(\boldsymbol{w}_{10},\boldsymbol{w}_{01},\boldsymbol{w}_{10})$ $\quad+\boldsymbol{f}_3(\boldsymbol{w}_{01},\boldsymbol{w}_{10},\boldsymbol{w}_{10})$ $\boldsymbol{R}_{21}=\begin{bmatrix}\frac{\mathrm{i}}{2\omega}\boldsymbol{\varphi}^T\boldsymbol{f}_{21}\\0\end{bmatrix}=\begin{bmatrix}\mathrm{i}\gamma\\0\end{bmatrix}$ $\Lambda_{21}=\mathrm{i}\omega$ $\mathbf{L}_{21}=\mathbf{K}+\Lambda_{21}^2\mathbf{M}$ $\boldsymbol{h}_{21}=\boldsymbol{f}_{21}+\mathbf{M}(\Lambda_{21}+\mathrm{i}\omega)\boldsymbol{\varphi}\mathrm{i}\gamma$ $\mathbf{L}_{21}\boldsymbol{w}_{21}+\boldsymbol{h}_{21}=\mathbf{0}$	$\boldsymbol{f}_{12}=\boldsymbol{f}_2(\boldsymbol{w}_{01},\boldsymbol{w}_{11})$ $\quad+\boldsymbol{f}_2(\boldsymbol{w}_{11},\boldsymbol{w}_{01})$ $\quad+\boldsymbol{f}_2(\boldsymbol{w}_{10},\boldsymbol{w}_{02})$ $\quad+\boldsymbol{f}_2(\boldsymbol{w}_{02},\boldsymbol{w}_{10})$ $\quad+\boldsymbol{f}_3(\boldsymbol{w}_{10},\boldsymbol{w}_{01},\boldsymbol{w}_{01})$ $\quad+\boldsymbol{f}_3(\boldsymbol{w}_{01},\boldsymbol{w}_{10},\boldsymbol{w}_{01})$ $\quad+\boldsymbol{f}_3(\boldsymbol{w}_{01},\boldsymbol{w}_{01},\boldsymbol{w}_{10})$ $\boldsymbol{R}_{12}=\begin{bmatrix}0\\\frac{-\mathrm{i}}{2\omega}\boldsymbol{\varphi}^T\boldsymbol{f}_{12}\end{bmatrix}=\begin{bmatrix}0\\-\mathrm{i}\gamma\end{bmatrix}$ $\Lambda_{12}=-\mathrm{i}\omega$ $\mathbf{L}_{12}=\mathbf{K}+\Lambda_{12}^2\mathbf{M}$ $\boldsymbol{h}_{12}=\boldsymbol{f}_{12}+\mathbf{M}(\Lambda_{12}-\mathrm{i}\omega)\boldsymbol{\varphi}(-\mathrm{i}\gamma)$ $\mathbf{L}_{12}\boldsymbol{w}_{12}+\boldsymbol{h}_{12}=\mathbf{0}$	$\boldsymbol{f}_{03}=\boldsymbol{f}_2(\boldsymbol{w}_{02},\boldsymbol{w}_{01})$ $\quad+\boldsymbol{f}_2(\boldsymbol{w}_{01},\boldsymbol{w}_{02})$ $\quad+\boldsymbol{f}_3(\boldsymbol{w}_{01},\boldsymbol{w}_{01},\boldsymbol{w}_{01})$ $\boldsymbol{R}_{03}=\mathbf{0}$ $\Lambda_{03}=-\mathrm{i}3\omega$ $\mathbf{L}_{03}=\mathbf{K}+\Lambda_{03}^2\mathbf{M}$ $\mathbf{L}_{03}\boldsymbol{w}_{03}+\boldsymbol{f}_{03}=\mathbf{0}$

Appendix B

Tensor notation

Using Einstein notation, the quadratic and cubic components of the nonlinear force are written as

$$f_2^i(\boldsymbol{a},\boldsymbol{b})=F_2^{ijk}a^jb^k \tag{B2}$$

$$f_3^i(\boldsymbol{a},\boldsymbol{b},\boldsymbol{c})=F_3^{ijkl}a^jb^kc^l, \tag{B3}$$

where $F_2\in\mathbb{R}^{n\times n\times n}$ and $F_3\in\mathbb{R}^{n\times n\times n\times n}$ are the tensors that describe, respectively, the quadratic and cubic nonlinearities. The vectors $\boldsymbol{a}$, $\boldsymbol{b}$, and $\boldsymbol{c}$ are the inputs of the nonlinear force. To avoid confusion with the subscripts denoting names, we used superscripts to identify entries of the corresponding entity (e.g., w_{10}^j denotes the j-th component of vector $\boldsymbol{w}_{10}$).

We use the tensor notation to rewrite the expressions for $\boldsymbol{f}_{20}$, $\boldsymbol{f}_{11}$, and $\boldsymbol{f}_{21}$:

$$f_{20}^i=F_2^{ijk}w_{10}^jw_{10}^k \tag{B4}$$

$$f_{11}^i=\left(F_2^{ijk}+F_2^{ikj}\right)w_{10}^jw_{01}^k \tag{B5}$$

$$\begin{aligned}f_{21}^i=&\left(F_2^{ijk}+F_2^{ikj}\right)w_{10}^jw_{20}^k\\&+\left(F_2^{ijk}+F_2^{ikj}\right)w_{01}^jw_{11}^k\\&+\left(F_3^{ijkl}+F_3^{iljk}+F_3^{ikljl}\right)w_{10}^jw_{10}^kw_{01}^l.\end{aligned} \tag{B6}$$

In this way, γ becomes

$$\gamma=\frac{1}{2\omega}\varphi^if_{21}^i. \tag{B7}$$

Tensor derivative

The partial derivatives of $f_{2,i}$ with respect to its input vectors are computed as

$$\frac{\partial f_2^i(\boldsymbol{a},\boldsymbol{b})}{\partial a^j}=F_2^{ijk}b^k \tag{B8a}$$

$$\frac{\partial f_2^i(\boldsymbol{a},\boldsymbol{b})}{\partial b^k}=F_2^{ijk}a^j. \tag{B8b}$$

In the same way, the partial derivatives of $f_{3,i}$ are written as

$$\frac{\partial f_3^i(\boldsymbol{a},\boldsymbol{b},\boldsymbol{c})}{\partial a^j}=F_3^{ijkl}b^kc^l \tag{B9a}$$

$$\frac{\partial f_3^i(\boldsymbol{a},\boldsymbol{b},\boldsymbol{c})}{\partial b^k} = F_3^{ijkl} a^j c^l \tag{B9b}$$

$$\frac{\partial f_3^i(\boldsymbol{a},\boldsymbol{b},\boldsymbol{c})}{\partial c^l} = F_3^{ijkl} a^j b^k. \tag{B9c}$$

Appendix C

Partial derivatives for sensitivities

To compute the adjoint Eqs. (17)– (20), the partial derivatives of γ with respect to the state variables $\boldsymbol{w}_{20}$, $\boldsymbol{w}_{11}$, $\boldsymbol{\varphi}$, and ω are required.

Using the tensor notation and substituting $\boldsymbol{w}_{10} = \boldsymbol{w}_{01} = \boldsymbol{\varphi}$, the partial derivatives of γ are written as

$$\frac{\partial \gamma}{\partial \omega} = -\frac{1}{2\omega^2}\varphi^i f_{21}^i = -\frac{1}{\omega}\gamma \tag{C10}$$

$$\frac{\partial \gamma}{\partial w_{20}^j} = \frac{1}{2\omega}\varphi^i \left(F_2^{ijk} + F_2^{ikj}\right)\varphi^k \tag{C11}$$

$$\frac{\partial \gamma}{\partial w_{11}^j} = \frac{1}{2\omega}\varphi^i \left(F_2^{ijk} + F_2^{ikj}\right)\varphi^k \tag{C12}$$

$$\begin{aligned}\frac{\partial \gamma}{\partial \varphi^j} = \frac{1}{2\omega}\Big[&f_{21}^j + \varphi^j \left(F_2^{ijk} + F_2^{ikj}\right) w_{20}^k \\ &+ \varphi^j \left(F_2^{ijk} + F_2^{ikj}\right) w_{11}^k \\ &+ 3\varphi^j \left(F_3^{ijkl} + F_3^{iljk} + F_3^{iklj}\right)\varphi^k \varphi^l\Big].\end{aligned} \tag{C13}$$

In the same way, the partial derivatives of $\boldsymbol{f}_{20}$ and $\boldsymbol{f}_{11}$ with respect to $\boldsymbol{\varphi}$ are

$$\frac{\partial f_{20}^i}{\partial \varphi^j} = \left(F_2^{ijk} + F_2^{ikj}\right) w_{20}^k \tag{C14}$$

$$\frac{\partial f_{11}^i}{\partial \varphi^j} = 2\left(F_2^{ijk} + F_2^{ikj}\right) w_{11}^k. \tag{C15}$$

These expressions (and in Eq. (23)) were finally validated using finite differences, passing the check with a tolerance of 10^{-5}. Notice that the adjoint sensitivity accuracy, along with the LS$\mathcal{M}$ accuracy, have already been extensively verified by Li (2024) and Li et al. (2023), respectively.

Appendix D

Topology optimization sensitivity analysis

The partial derivative of the mass matrix $\mathbf{M}$ is computed using the chain rule:

$$\frac{\partial \mathbf{M}}{\partial \mu_e} = \sum_{j=1}^{N} \frac{\partial \mathbf{M}}{\partial \hat{\mu}_j} \frac{\partial \hat{\mu}_j}{\partial \bar{\mu}_j} \frac{\partial \bar{\mu}_j}{\partial \tilde{\mu}_j} \frac{\partial \tilde{\mu}_j}{\partial \mu_e}. \tag{D16}$$

The partial derivatives in Eq. (D16) are obtained by differentiating Eqs. (25), (27)–(29):

$$\frac{\partial \tilde{\mu}_j}{\partial \mu_e} = \begin{cases} \frac{w_{e,j}}{\sum_{l\in\mathcal{N}_j} w_{l,j}} & \text{if } e \in \mathcal{N}_j \\ 0 & \text{otherwise} \end{cases} \tag{D17}$$

$$\frac{\partial \bar{\mu}_j}{\partial \tilde{\mu}_j} = \beta \frac{1 - \tanh^2\left(\beta(\tilde{\mu}_j - \eta)\right)}{\tanh\left(\beta\eta\right) + \tanh\left(\beta(1-\eta)\right)} \tag{D18}$$

$$\frac{\partial \hat{\mu}_j}{\partial \bar{\mu}_j} = p(1 - \hat{\mu}_0)\bar{\mu}_j^{p-1} \tag{D19}$$

$$\frac{\partial \mathbf{M}}{\partial \hat{\mu}_j} = \mathbf{M}_j, \tag{D20}$$

where $\mathbf{M}_j$ is the element mass matrix of element j. The same expressions are used to obtain the derivatives of $\mathbf{K}$, F_2, and F_3.

Acknowledgements The authors acknowledge the financial support of STMicroelectronics. ML acknowledges the financial support of the National Natural Science Foundation of China (No. 12302014)

Author contributions Matteo Pozzi: conceptualization, methodology, formal analysis, investigation, software development, and writing-original draft preparation. Jacopo Marconi: conceptualization, methodology, formal analysis, investigation, software development, and writing-original draft preparation. Shobhit Jain: validation, visualization, and writing-review & editing. Mingwu Li: validation, visualization, and writing-review & editing. Francesco Braghin: supervision and funding acquisition. All authors reviewed and approved the final manuscript.

Funding Open access funding provided by Politecnico di Milano within the CRUI-CARE Agreement. STMicroelectronics (Award Number 4000614871). National Natural Science Foundation of China (No. 12302014)

Declarations

Conflict of interest On behalf of all authors, the corresponding author states that there is no conflict of interest.

Replication of results YetAnotherFEcode (Jain et al. 2022) was used to implement the topology optimization routine and to obtain the numeri-

cal examples. No datasets were generated or analyzed during the current study. All relevant results are included in the published article.

References

Acar C, Shkel A (2009) MEMS vibratory gyroscopes. Springer. https://doi.org/10.1007/978-0-387-09536-3

Allaire G, Jouve F, Toader AM (2004) Structural optimization using sensitivity analysis and a level-set method. J Comput Phys 194:363–393. https://doi.org/10.1016/J.JCP.2003.09.032

Bellet R, Cochelin B, Herzog P, Mattei PO (2010) Experimental study of targeted energy transfer from an acoustic system to a nonlinear membrane absorber. J Sound Vib 329(14):2768–2791. https://doi.org/10.1016/j.jsv.2010.01.029

Bendsøe MP, Sigmund O (1999) Material interpolation schemes in topology optimization. Arch Appl Mech 69:635–654. https://doi.org/10.1007/S004190050248

Bendsøe MP, Sigmund O (2004) Topology optimization: theory, methods, and applications. Springer, Berlin Heidelberg. https://doi.org/10.1007/978-3-662-05086-6

Breunung T, Haller G (2018) Explicit backbone curves from spectral submanifolds of forced-damped nonlinear mechanical systems. Proc R Soc A: Math Phys Eng Sci 474(2213):20180083. https://doi.org/10.1098/rspa.2018.0083

Choi W, Park G (2002) Structural optimization using equivalent static loads at all time intervals. Comput Methods Appl Mech Eng 191(19):2105–2122. https://doi.org/10.1016/S0045-7825(01)00373-5

Dalklint A, Wallin M, Tortorelli DA (2020) Eigenfrequency constrained topology optimization of finite strain hyperelastic structures. Struct Multidisc Optim 61:2577–2594. https://doi.org/10.1007/s00158-020-02557-9

Dankowicz H, Schilder F (2013) Recipes for continuation. Society for Industrial and Applied Mathematics, Philadelphia

de la Llave R, Kogelbauer F (2019) Global persistence of lyapunov subcenter manifolds as spectral submanifolds under dissipative perturbations. SIAM J Appl Dyn Syst 18(4):2099–2142. https://doi.org/10.1137/18M1210344

Detroux T, Noël JP, Kerschen G (2021) Tailoring the resonances of nonlinear mechanical systems. Nonlinear Dyn 103:3611–3624. https://doi.org/10.1007/s11071-020-06002-w

Dou S, Jensen JS (2015) Optimization of nonlinear structural resonance using the incremental harmonic balance method. J Sound Vib 334:239–254. https://doi.org/10.1016/j.jsv.2014.08.023

Dou S, Jensen JS (2016) Optimization of hardening/softening behavior of plane frame structures using nonlinear normal modes. Comput Struct 164:63–74. https://doi.org/10.1016/j.compstruc.2015.11.001

Dou S, Strachan BS, Shaw SW, Jensen JS (2015) Structural optimization for nonlinear dynamic response. Phil Trans R Soc A: Math Phys Eng Sci 373:20140408. https://doi.org/10.1098/rsta.2014.0408

Giannini D, Braghin F, Aage N (2020) Topology optimization of 2D in-plane single mass MEMS gyroscopes. Struct Multidisc Optim 62:2069–2089. https://doi.org/10.1007/s00158-020-02595-3

Giannini D, Aage N, Braghin F (2022) Topology optimization of MEMS resonators with target eigenfrequencies and modes. Eur J Mech A Solids 91:104352. https://doi.org/10.1016/J.EUROMECHSOL.2021.104352

Giannini D, Schevenels M, Reynders EP (2024) Topology optimization design of multi-modal resonators for metamaterial panels with maximized broadband vibroacoustic attenuation. J Sound Vib. https://doi.org/10.1016/j.jsv.2024.118691

Guo X, Zhang W, Zhong W (2014) Doing topology optimization explicitly and geometrically—a new moving morphable components based framework. J Appl Mech 10(1115/1):4027609

Haller G, Ponsioen S (2016) Nonlinear normal modes and spectral submanifolds: existence, uniqueness and use in model reduction. Nonlinear Dyn 86(3):1493–1534. https://doi.org/10.1007/s11071-016-2974-z

Jain S, Haller G (2022) How to compute invariant manifolds and their reduced dynamics in high-dimensional finite element models. Nonlinear Dyn 107(2):1417–1450. https://doi.org/10.1007/s11071-021-06957-4

Jain S, Marconi J, Tiso P (2022) YetAnotherFEcode, v1.3.0. https://doi.org/10.5281/zenodo.7313486

Jain S, Thurnher T, Li M, Haller G (2023) SSMTool: computation of invariant manifolds in high-dimensional mechanics problems, v2.4. https://doi.org/10.5281/zenodo.8171657

Kelley A (1969) Analytic two-dimensional subcenter manifolds for systems with an integral. Pac J Math 29:335–350. https://doi.org/10.2140/pjm.1969.29.335

Kerschen G, Viguié R, Golinval JC, Peeters M, Sérandour G (2008) Nonlinear normal modes, Part II: toward a practical computation using numerical continuation techniques. Mech Syst Signal Process 23(1):195–216. https://doi.org/10.1016/j.ymssp.2008.04.003

Kerschen G, Peeters M, Golinval JC, Vakakis AF (2009) Nonlinear normal modes, Part I: a useful framework for the structural dynamicist. Mech Syst Signal Process 23(1):170–194. https://doi.org/10.1016/j.ymssp.2008.04.002

Kim TS, Kim YY (2000) Mac-based mode-tracking in structural topology optimization. Comput Struct 74:375–383. https://doi.org/10.1016/S0045-7949(99)00056-5

Kim YI, Park GJ (2010) Nonlinear dynamic response structural optimization using equivalent static loads. Comput Methods Appl Mech Eng 199(9):660–676. https://doi.org/10.1016/j.cma.2009.10.014

Krack M, Gross J (2019) Harmonic balance for nonlinear vibration problems. Mathematical Engineering, Springer International Publishing, Cham. https://doi.org/10.1007/978-3-030-14023-6

Lee HA, Park GJ (2015) Nonlinear dynamic response topology optimization using the equivalent static loads method. Comput Methods Appl Mech Eng 283:956–970. https://doi.org/10.1016/j.cma.2014.10.015

Li M (2024) Explicit sensitivity analysis of spectral submanifolds of mechanical systems. Nonlinear Dyn. https://doi.org/10.1007/s11071-024-09947-4

Li M, Jain S, Haller G (2023) Model reduction for constrained mechanical systems via spectral submanifolds. Nonlinear Dyn 111(10):8881–8911. https://doi.org/10.1007/s11071-023-08300-5

Li M, Thurnher T, Xu Z, Jain S (2025) Data-free non-intrusive model reduction for nonlinear finite element models via spectral submanifolds. Comput Methods Appl Mech Eng 434:117590. https://doi.org/10.1016/j.cma.2024.117590

Li Q, Sigmund O, Jensen JS, Aage N (2021) Reduced-order methods for dynamic problems in topology optimization: a comparative study. Comput Methods Appl Mech Eng 387:114149. https://doi.org/10.1016/j.cma.2021.114149

Li Q, Wu Q, Dou S, Wang J, Liu S, Chen W (2022) Nonlinear eigenvalue topology optimization for structures with frequency-dependent material properties. Mech Syst Signal Process 170:108835. https://doi.org/10.1016/j.ymssp.2022.108835

Lu S, Zhang Z, Guo H, Park GJ, Zuo W (2021) Nonlinear dynamic topology optimization with explicit and smooth geometric outline via moving morphable components method. Struct Multidisc Optim 64(4):2465–2487. https://doi.org/10.1007/s00158-021-03000-3

Marconi J, Tiso P, Braghin F (2020) A nonlinear reduced order model with parametrized shape defects. Comput Methods Appl Mech Eng 360:112785. https://doi.org/10.1016/j.cma.2019.112785

Marconi J, Bonaccorsi G, Giannini D, Falorni L, Braghin F (2021a) Exploiting nonlinearities for frequency-matched MEMS gyroscopes tuning. In: 2021 IEEE international symposium on inertial sensors and systems (INERTIAL). IEEE, pp 1–4. https://doi.org/10.1109/INERTIAL51137.2021.9430478

Marconi J, Tiso P, Quadrelli DE, Braghin F (2021b) A higher-order parametric nonlinear reduced-order model for imperfect structures using Neumann expansion. Nonlinear Dyn 104(4):3039–3063. https://doi.org/10.1007/s11071-021-06496-y

Pozzi M, Bonaccorsi G, Braghin F (2023) A temperature-robust level-set approach for eigenfrequency optimization. Struct Multidisc Optim. https://doi.org/10.1007/s00158-023-03622-9

Pozzi M, Bonaccorsi G, Kim HA, Braghin F (2023) Robust structural optimization in presence of manufacturing uncertainties through a boundary-perturbation method. Struct Multidisc Optim 66:120. https://doi.org/10.1007/s00158-023-03573-1

Pozzi M, Marconi J, Jain S, Braghin F (2024) Backbone curve tailoring via Lyapunov subcenter manifold optimization. Nonlinear Dyn 112:15719–15739. https://doi.org/10.1007/s11071-024-09881-5

Pozzi M, Marconi J, Jain S, Li M, Braghin F (2025) Adjoint sensitivities for the optimization of nonlinear structural dynamics via spectral submanifolds. https://arxiv.org/abs/2503.17431

Qalandar KR, Strachan BS, Gibson B, Sharma M, Ma A, Shaw SW, Turner KL (2014) Frequency division using a micromechanical resonance cascade. Appl Phys Lett 105(24):244103. https://doi.org/10.1063/1.4904465

Saccani A, Marconi J, Tiso P (2022) Sensitivity analysis of nonlinear frequency response of defected structures. Nonlinear Dyn. https://doi.org/10.1007/s11071-022-08064-4

Schiwietz D, Hörsting M, Weig EM, Degenfeld-Schonburg P, Wenzel M (2024) Shape optimization of eigenfrequencies in MEMS gyroscopes. https://arxiv.org/abs/2402.05837

Schiwietz D, Hörsting M, Weig EM, Wenzel M, Degenfeld-Schonburg P (2025) Shape optimization of geometrically nonlinear modal coupling coefficients: an application to MEMS gyroscopes. Sci Rep 15:95412. https://doi.org/10.1038/s41598-025-95412-0

Silva OM, Neves MM, Lenzi A (2019) A critical analysis of using the dynamic compliance as objective function in topology optimization of one-material structures considering steady-state forced vibration problems. J Sound Vib 444:1–20. https://doi.org/10.1016/j.jsv.2018.12.030

Svanberg K (1987) The method of moving asymptotes—a new method for structural optimization. Int J Numer Meth Eng 24:359–373. https://doi.org/10.1002/nme.1620240207

Thurnher T, Haller G, Jain S (2024) Nonautonomous spectral submanifolds for model reduction of nonlinear mechanical systems under parametric resonance. Chaos: Interdisc J Nonlin Sci 34(7):073127. https://doi.org/10.1063/5.0168431

Tiso P, Mahdiabadi MK, Marconi J (2021) Modal methods for reduced order modeling. De Gruyter, Berlin, pp 97–138. https://doi.org/10.1515/9783110498967-004

Touzé C, Vizzaccaro A, Thomas O (2021) Model order reduction methods for geometrically nonlinear structures: a review of nonlinear techniques. Nonlinear Dyn 105(2):1141–1190. https://doi.org/10.1007/s11071-021-06693-9

Townsend S, Grigg S, Picelli R, Featherston C, Kim HA (2019) Topology optimization of vibrational piezoelectric energy harvesters for structural health monitoring applications. J Intell Mater Syst Struct 30(18–19):2894–2907. https://doi.org/10.1177/1045389X19873392

Vakakis AF, Gendelman OV, Bergman LA, Mojahed A, Gzal M (2022) Nonlinear targeted energy transfer: state of the art and new perspectives. Nonlinear Dyn 108(2):711–741. https://doi.org/10.1007/s11071-022-07216-w

Wang F, Lazarov BS, Sigmund O (2011) On projection methods, convergence and robust formulations in topology optimization. Struct Multidisc Optim 43:767–784. https://doi.org/10.1007/s00158-010-0602-y

Wang MY, Wang X, Guo D (2003) A level set method for structural topology optimization. Comput Methods Appl Mech Eng 192:227–246. https://doi.org/10.1016/S0045-7825(02)00559-5

Xie YM, Steven GP (1993) A simple evolutionary procedure for structural optimization. Comput Struct 49:885–896. https://doi.org/10.1016/0045-7949(93)90035-C

Yang X, Li Y (2013) Topology optimization to minimize the dynamic compliance of a bi-material plate in a thermal environment. Struct Multidisc Optim 47:399–408. https://doi.org/10.1007/s00158-012-0831-3

Yang X, Li Y (2014) Structural topology optimization on dynamic compliance at resonance frequency in thermal environments. Struct Multidisc Optim 49:81–91. https://doi.org/10.1007/s00158-013-0961-2

Zhang W, Baskaran R, Turner KL (2002) Effect of cubic nonlinearity on auto-parametrically amplified resonant MEMS mass sensor. Sens Actuators, A 102(1):139–150. https://doi.org/10.1016/S0924-4247(02)00299-6